Toward the Detection of Oil Spills in Newly Formed Sea Ice Using C-Band Multipolarization Radar

Elvis Asihene, *Graduate Student Member, IEEE*, Durell S. Desmond, Madison L. Harasyn, David Landry, Cathrin Veenaas, Amirbahador Mansoori, *Student Member, IEEE*, Mark Christopher Fuller, Gary Stern, David G. Barber, Colin Gilmore, *Senior Member, IEEE*, and Dustin Isleifson, *Senior Member, IEEE*

***Abstract*— Oil spills in the Arctic are becoming more likely as shipping traffic increases in response to climate-related sea ice loss. To improve oil spill detection capability, we used a controlled mesocosm to analyze the multipolarized C-band backscatter response of oil in newly formed sea ice (NI). Artificial sea ice was grown in two cylindrical tubs at the Sea-ice Environmental Research Facility, University of Manitoba. The sea ice physical characteristics, including surface roughness, thickness, temperature, and salinity, were measured before and after oil injection below the ice sheet. Time-series C-band radar backscatter measurements detected the differences in the sea ice evolution and oil migration to the sea ice surface in the oil-contaminated tub, which was compared to uncontaminated ice in a control tub. Immediately prior to the presence of oil on the ice surface, the copolarized backscatter is increased by 13-dB local maximum, while the cross-polarized backscatter is decreased by 9-dB. Ice physical properties suggest that the local backscatter maximum and minimum, which occurred immediately before oil migrated onto the surface, were related to a combination of brine and oil upward migration. The findings of this work provide a baseline data interpretation for oil detection in the Arctic Ocean using current and future C-band multipolarization radar satellites.**

***Index Terms*— Arctic, detection, oil spill, radar backscatter, sea ice.**

I. Introduction

IN RECENT decades, the Arctic marine environment has become economically attractive for shipping and hydrocarbon exploration due to climate-related sea ice loss [1]–[3]. These economic activities are associated with a high risk of oil spills [4], which have adverse effects on fauna, flora, and surrounding communities. Following the Deepwater Horizon oil spill, stakeholders in the Canadian Arctic sector, including indigenous communities, private investors, and government agencies, emphasized the critical need for immediate preparedness and contingency planning in the event of an Arctic oil spill [5]. However, the extreme cold, darkness, remoteness, and sparsely distributed infrastructure (for example, transportation, communication, equipment, and waste management) in the Arctic region make operations and logistics difficult [6]–[8]. Remote sensing can a play major role in solving these challenges by providing information about the physical state of ice conditions and enabling early detection of oil spills without physically involving responders.

Detection of the location and extent of an oil spill is necessary to optimize countermeasures and can be achieved by mounting a suite of sensors on both spaceborne and airborne platforms [9], [10]. Spaceborne platforms are highly reliable for rapid identification of pollution with the wider area but are disadvantaged by longer repeat visit cycles allowing for significant changes to go undetected between image acquisitions [9]. Airborne platforms, on the other hand, are able to collect high temporal resolution data over a much smaller region. Optical and radar sensors have been tested for their capabilities and limitations in spotting oil slicks on both airborne and spaceborne platforms [11]. In often dark and overcast Arctic conditions, radar sensors transmit and receive signals in frequencies independent of weather conditions and solar illumination, which could be useful for oil-in-sea ice remote sensing.

Currently, spaceborne and airborne synthetic aperture radars (SARs) are operationally monitoring marine oil contamination [10]; however, the process and techniques are confused by distributed sea ice. Single-polarization SAR has been used to detect the smoothing of capillary waves on the ocean surface caused by the presence of oil, which results in an area of decreased backscatter [12]. The presence of sea ice alters the distribution of oil so that oil exists below, within, and above the ice [6]. Sea ice types, such as frazil, grease ice, and nilas, complicate the detection of oil spills that are often indistinguishable from newly formed sea ice (NI) in SAR imagery [13]. Recent studies used multipolarization SAR to enhance the low backscatter between NI and oil-contaminated sea ice [13]–[16]. The results showed the

Manuscript received June 16, 2021; revised September 22, 2021; accepted October 15, 2021. Date of publication October 27, 2021; date of current version February 14, 2022. This work was supported in part by GENICE, in part by Research Manitoba, in part by Canada Research Chair (CRC) Programs, in part by the Natural Sciences and Engineering Research Council (NSERC) of Canada, in part by the Canada Foundation for Innovation (CFI), and in part by the University of Manitoba GETS Program. *(Corresponding author: Elvis Asihene.)*

Elvis Asihene, Durell S. Desmond, Madison L. Harasyn, David Landry, Gary Stern, and David G. Barber are with the Centre for Earth Observation Science (CEOS), University of Manitoba, Winnipeg, MB R3T 5V6, Canada (e-mail: asihenee@myumanitoba.ca).

Cathrin Veenaas is with the Centre for Earth Observation Science (CEOS), University of Manitoba, Winnipeg, MB R3T 5V6, Canada, and also with the Department of Chemistry, Örebro University, SE-701 82 Örebro, Sweden.

Amirbahador Mansoori and Colin Gilmore are with the Department of Electrical and Computer Engineering, University of Manitoba, Winnipeg, MB R3T 5V6, Canada.

Mark Christopher Fuller is with the Cryosphere and Climate Research Group, Department of Geography, University of Calgary, Calgary, AB T2N 1N4, Canada.

Dustin Isleifson is with the Centre for Earth Observation Science (CEOS) and the Department of Electrical and Computer Engineering, University of Manitoba, Winnipeg, MB R3T 5V6, Canada.

Digital Object Identifier 10.1109/TGRS.2021.3123908

potential for differentiating oil spills from the NI types, but the validation of these theoretical studies is still a problem in the Arctic, as regulations prohibit deliberate, field-scale oil spills [7]. Another challenge to address is the need for calibration accuracy from satellite and aircraft monitoring, which can lead to misinterpretation of oil spills. Even with a surface-based multipolarization SAR, a recommendation from [15] cautioned future experiments against using the data for comparative analysis due to the need for calibration. Simulating the Arctic region in a controlled mesocosm with a well-calibrated surface-based scatterometer can aid in overcoming some of these restraints.

Building on previous experiments [17]–[19], the overarching objective of this research is to establish how the physical and thermodynamic properties of oil-contaminated NI impact the C-band backscatter and to evaluate how these results can be used to remotely detect oil in newly forming sea ice. The C-band multipolarization radar will be used in this study to allow for future comparison and validation with existing C-band multipolarization SAR satellites (e.g., Canada's RADARSAT 2 and RCM, as well as the European Space Agency's Sentinel 1). In addition, because the C-band is the optimal frequency for monitoring sea ice all season [20], it is expected to be effective at discriminating NI types that are prevalent during freeze-up periods from oil spill events. In this work, we answer the following two questions:

1) What are the relationships between the physical, thermodynamic, and microwave C-band scattering properties of newly forming sea ice in our mesocosm leading up to and following an oil spill event?
2) How does the presence of a layer of oil on seawater influence the growth, physical properties, and microwave C-band scattering properties of newly forming sea ice?

We address these questions and meet our overarching objective by conducting experiments on oil-contaminated sea ice at the Sea-ice Environmental Research Facility (SERF), located at the University of Manitoba, Winnipeg, MB, Canada. Section II provides a short background for the understanding of oil behavior in NI and the C-band backscatter response. Section III outlines the materials and methods, while Section IV presents the experimental results. Section V uses all the results from Section IV to discuss the time-series evolution of C-band backscatter from sea ice, prior to and after oil injection. We conclude with a summary and recommendations in Section VI.

II. Theoretical Background

It is well-established that microwave scattering and propagation in sea ice are governed by the dielectric properties of sea ice, and the scattering response is dependent upon the physical and thermodynamic states of the ice [21]. The radar backscatter response of sea ice, which can be used to determine its state, is both frequency- and polarization-dependent [20]. Moreover, the time-series evolution of sea ice backscatter has been a valuable proxy of change in sea ice state, including initial formation processes, frost flower growth, and ablation of snow cover, to name a few [20]. The introduction of oil into a sea ice environment complicates the interpretation of remote sensing data because the dielectric properties of oil-contaminated sea ice differ from that of uncontaminated sea ice [22].

A. Physical Properties of Newly Formed Sea Ice

Sea ice is an inhomogeneous mixture of liquid brine (dissolved salts) pockets, air pockets, and solid salts in a pure ice matrix. The three primary physical properties of NI that is relevant to radar remote sensing are temperature, salinity (amount of dissolved salts), and surface features [23]. Examples of surface features that influence radar backscattering are the roughness of bare ice surface or the presence of frost flowers, snow, and saline layers on the ice surface [24]. On a small scale, the surface roughness of sea ice can be statistically characterized by the standard deviation (root-mean-square (rms) height) and the correlation length from the variations around the mean ice surface elevation [25]. Under calm conditions, bare NI is usually relatively smooth because there is minimal to zero degrees of deformation during its growth cycle [21]. Frost flowers are vapor-condensed ice crystals that are highly saline due to the brine wicking from the NI surface [26], and as frost flowers cover the NI surface, the surface roughness increases [20].

B. Oil Behavior in Newly Formed Sea Ice

The behavior of oil in ice-covered waters is influenced by the scenario in which the spill occurs (on the surface or under the ice sheet), the properties of the oil, and the ambient sea ice conditions [6], [27]. The oil that is released below the ice, under calm conditions and freezing temperatures, enters the seawater column as droplets [28], [29]. When the oil reaches the ice–water interface, the oil spreads and tends to migrate upward because it is less dense than the ice above. Due to the interspersed granular brine pockets at the uppermost layer [30], the rising oil becomes encapsulated within the NI sheet [28]–[30], and the oil's insulating properties may slow the rate of ice growth beneath the oil layer [31], [32]. If the oil volume fraction is greater or equal to 2%, the rate of upward migration increases [32], [33]. Moreover, if the ambient sea ice temperature increases, the rate of upward oil migration through brine channels accelerates [28]–[30]. Once the oil migrates to the air–ice interface, it wets and spreads over the surface of the sea ice, resulting in a smoothing of the surface.

C. C-Band Backscatter Response of Newly Formed Sea Ice

There are limited studies of C-band backscatter from NI (see [20], [34]–[36], and references therein). In microwave remote sensing, the normalized radar cross section (NRCS) is often used to describe the backscattering behavior of sea ice. Using the formulation in [37], the NRCS, σ° (in a monostatic mode), can be expressed as

$$\sigma^{\circ}_{qp} = \lim_{R\to\infty} \frac{4\pi R^2}{A} \left[\frac{\langle S^{\mathrm{sc}}_p \rangle}{\langle S^{\mathrm{in}}_q \rangle} \right] \tag{1}$$

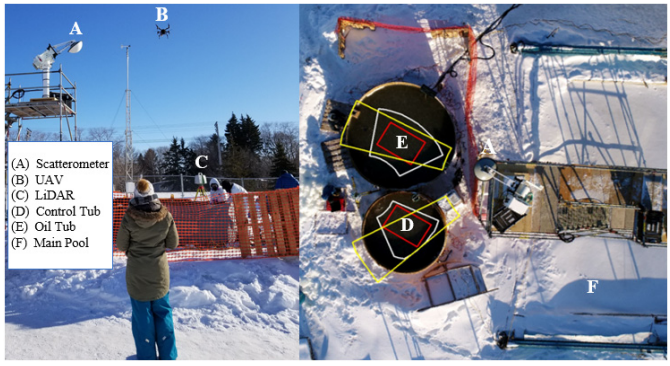

Fig. 1. Experiment setup and data acquisition. The overlain polygons on each tub correspond to scatterometer footprint (yellow), LiDAR footprint (white), and the area extracted for surface roughness statistics (red). Both images were captured about the 10th hour of the phase-one experiment (sea ice growth state is dark nilas).

where R, A, S^{sc}, and S^{in} represent the distance between the sea ice and radar antenna, the area of illumination, the scattered power density, and the incident power density, respectively. The subscripts q and p denote the linearly transmitted and received polarizations that are orthogonal to each other as vertical (V) or horizontal (H) components, respectively. $\langle\cdot\rangle$ represents the spatial ensemble averaging operator. For NI, the dominant scattering mechanism is mainly surface scattering because the topmost layer is highly saline. If the surface is covered with frost flowers, the NRCS is expected to increase by 6-dB [38]. When oil forms a thin layer over the growing NI sheet, the NRCS is expected to decrease [18].

III. Materials and Methods

A. Experimental Setup

An oil-in-sea ice mesocosm experiment was undertaken at SERF in February 2020. This experiment was conducted in two isolated sets of cylindrical tubs (hereafter referred to as "control tub" and "oil tub") that are physically separate from the western side of the main pool (see Fig. 1). The control tub (with fiberglass insulation) has a radius of 1.5-m and a depth of 1.0-m, whereas the uninsulated oil tub has a radius of 2.0-m and a depth of 1.0-m. Both tubs were fit with polyvinyl chloride pipes that served as placeholders for thermocouple strings. A scaffold tower was set up beside the tubs to allow us to mount our radar instrument and give an overhead view of the experimental tubs. The experiment was performed in two phases (February 7/8 and 12/13, respectively). Throughout both experiments, we collected data from physical sampling and *in situ* measurements, Light Detection and Ranging (LiDAR) and unmanned aerial vehicle (UAV) measurements, and scatterometer measurements. We selected an experiment time period during which the forecast air temperatures were colder than −20 °C for both phases of the experiment. In addition to manual observations of water, sea ice, and air variables, a meteorological station located 15-m away from the tubs provided automated meteorological conditions, including atmospheric pressure and temperature, wind speed, relative humidity, and radiative fluxes (downwelling shortwave/longwave).

Phase-one experiment examined oil released under existing sea ice. In both tubs, ice was grown concurrently from uncontaminated seawater (32.8 PSU [40]) under ambient temperature and quiescent conditions (using similar approaches as in [17]–[19]). The water in the tubs was heated and circulated to maintain an open water condition until the experiment start, which occurred at midnight on February 7, 2020. After 12.5-h of ice growth (>4-cm thick), 6-L of light crude oil (supplied by Tundra Oil and Gas Ltd.) was then pumped under the sea ice of the experimental oil tub through a hole that was carefully drilled in the ice. The oil dispersed and spread across ice–water interface, which was visible in photographs taken from the scaffold tower (note that the ice was thin, and the dark oil was seen through the sea ice).

Phase-two experiment evaluated sea ice formation in oil-contaminated synthetic seawater. Heaters in both tubs melted the existing sea ice developed in the first phase, and sea ice then evolved from the oil-contaminated seawater to evaluate the effect of oil on sea ice growth.

All personnel involved in the physical sampling of oil-contaminated sea ice were trained in the handling of oil products and wore coverall suits and passive respirators during the experiment. Safety was of paramount importance throughout the experiment, and we used an H2S sensor to monitor the area. In addition, to prohibit untrained personnel away from the tubs, we placed a fence (shown in orange—Fig. 1) around the area.

B. Physical Sampling Methods

Ice cores were extracted using either a Kovacs Enterprise Mark II coring system (9-cm diameter) or a boning saw (rectangular dimensions) [see Fig. 2] and stored in sealable plastic bags. To check for surface wetness, we used Kimwipe and gently touched it to the surface. We noted the occurrence or the absence of moisture-wicking. In addition, ice surface scrapings of approximately 0.5-cm thickness and 4-L subsurface water samples were collected. The water samples were taken ∼10–20 cm below the ice by submerging a sterilized glass container under previously cored holes. Ice core and surface samples were taken with sufficient spatial variability, corresponding to the radar footprint, and we were cautious to ensure that our physical sampling locations did not coincide with the radar scan region (see Section III-D). At the end of the phase-one experiment, we destructively sampled the sea ice in the middle of the tub [see Fig. 2 (upper right)] coinciding with the radar scan footprint. All samples were stored in a freezer for later analysis, as shown in Table I. A heating coil, a thermocouple string, and a temperature data logger were installed in each tub. Every minute, at 2.5-cm intervals, the thermocouple string was used to collect *in situ* temperature profiles of air, ice volume, and water, and the data were averaged every 30 min. The total length of the thermocouple string was 37.5-cm: 10-cm above the ice surface and the rest below the air–ice interface through the ice volume into the seawater column. It should be noted that the sun directly illuminated several of the thermocouples during part of the day, resulting in erroneous measurements;

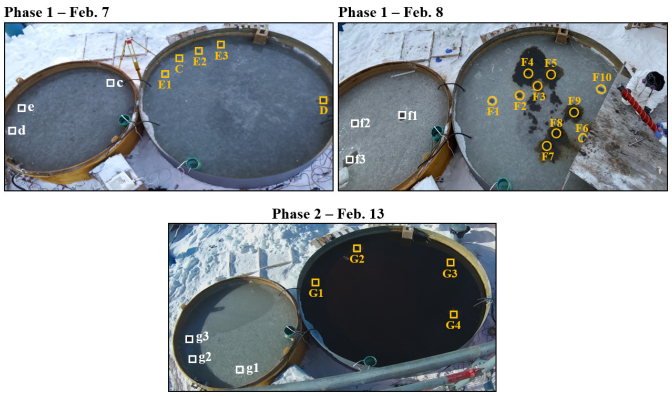

Fig. 2. Ice core extraction during phase 1 and 2 experiments. The letters on each tub identified the various locations where ice cores were collected using a drilling system (represented by circle symbols) and a boning saw (represented by square symbols). The white and orange colors denote ice cores from the control and oil tubs, respectively. On February 7, 2020 (Upper Left), phase 1 samples—C/c, D/d, and E(1–3)/e—were collected at 8 A.M., 11 A.M., and 2 P.M., respectively; on February 8, 2020 (Upper Right), phase 1 samples—F(1–10)/f(1–3)—were collected at around 11 A.M.; and on February 13, 2020 (bottom), phase 2 samples—G(1–4)/g(1–3)—were collected at around 10 A.M.

however, these errors do not significantly affect the ice core sample temperatures compared to our field temperature measurements.

After extraction, the length of each ice core was measured. The cores from the February 8 sampling session were 7.5- and 8-cm thick in the oil and control tubs, respectively, and were cut in two parts: air–ice interface to 5-cm, and 5–7.5 cm for the oil tub; air–ice interface to 5-cm, and 5–8 cm for the control tub. Each sample was melted, weighed on a calibrated mass balance, and the total volume was determined using a volumetric cylinder. Finally, the sample was transferred to a separatory funnel. A portion of hexane (hexanes Optima grade, >99.9% sum C6 hydrocarbons, Fisher Chemical, Fair Lawn, NJ, USA) corresponding to 20% of the sample volume was added to the sample bag for rinsing and subsequently added to the separatory funnel. The funnel was shaken, and the water phase and hexane phase were separated. Water was added to the separatory funnel again, while the hexane phase, containing the oil fraction, was added to a boiling flask. This procedure was repeated at least three times until the hexane phase was clear.

Bulk salinity in the water phase was measured using a conductivity meter (Orion Star 212, Thermo Scientific). The brine volume fractions (V_b/V) of each ice section were then subsequently calculated as follows [39], [41] (2)–(4), as shown at the bottom of the next page, where (V_a/V), S_b, T_{si}, and P_i represent the air volume fraction, bulk salinity (PSU), *in situ* (volume) temperature (°C), and pure ice density (kg/m^3), respectively. F_1 and F_2 are mathematical functions that depend on T_{si} between −2 °C and −22.9 °C. Because the volume of air pockets within NI types is extremely small [42], we assumed (V_a/V) to be negligible, simplifying $[1-(V_a/V)]$ to 1.

The hexane phase was evaporated using a rotary evaporator at 40 °C and 290 mbar until it reached 1–2 mL. The sample was transferred to a centrifuge tube and further evaporated at room temperature under a stream of nitrogen until no change in volume was observed. Finally, the volume of the oil fraction was determined visually by adding known amounts of water to a centrifuge tube and comparing the levels visually. This procedure was previously tested in a blind test and proved to be accurate to ±10 μL [43].

C. LiDAR and UAV Methods

Two terrestrial LiDAR point cloud datasets were collected on February 7, 2020, using a Leica C10 ScanStation sensor. The first series of scans were conducted 3-h prior to the oil injection, while the second series was collected approximately 30 min after the oil injection procedure. As a whole, these point cloud data include cartesian coordinate measurements relative to the stationary sensor position, intensity values from each point return, and RGB values associated with the digital imagery captured by the sensor. The scan station was positioned in a fixed location adjacent to the western side of the tubs and was set on a tripod at 1.85-m above the ground surface. This positioning was consistent throughout the day for both sets of scans. Prior to the high-resolution scans of the ice surface, a 360° field-of-view scan was conducted with a scanner configuration of 0.01-m point spacing at a 10-m range. During the high-resolution area scans over the tubs, the scanner was configured to collect data points at a 0.002-m spacing at the 10-m range, as described in [24], as an optimal configuration for this type of analysis. All point cloud data were stored in-field and were later exported to CloudCompare software [44], where initial filtering, removal of outlier points, and 2 × 2 mm regularization were conducted. Surface roughness parameters, such as rms height σ_h and correlation length L_c, were calculated for a rectangular subset of the LiDAR footprint area, following the methods in [25], [37], [45]

$$\sigma_h = \sqrt{\frac{1}{N-1}\sum_{k=1}^{N}\left|h(k)-\tilde{h}\right|^2} \tag{5}$$

$$L_c = |\delta| \text{ at } C(\delta)e^{-1} \tag{6}$$

where h is the height relative to the mean ice surface elevation. The subscript k represents the sample point of h, and N is the total number of sample points. Note that $\tilde{h}$ represents the mean value of h. With regards to (6), the autocovariance function is $C(\delta) = \langle h(x,y), h(\acute{x},\acute{y})\rangle/{\sigma_h}^2$, and the symbol $\langle\cdot\rangle$ denotes the autocovariance operator. The lag distance between h at location (x, y) and $(\acute{x}, \acute{y})$ is given as $\delta = ((x-\acute{x})^2 + (y-\acute{y})^2)^{1/2}$, and L_c is the absolute value of δ for which $C(\delta) = e^{-1}$.

As time progressed, the cold ambient environment exceeded the operation standards of our LiDAR sensor, thus resulting in the need to shift focus to a complementary approach. Aerial UAV-based optical imagery was collected on February 7 and 8 using a DJI Phantom 4 Pro with a standard 20-MP optical camera (see Fig. 1, labeled B). The UAV was flown at an altitude of 5-m in a manual gridded flight path to capture imagery with at least an 80% across- and along-track overlaps, to allow for photogrammetric analysis. Ground control points (GCPs) were positioned on the ice surface

TABLE I
NUMBERS OF SAMPLES COLLECTED PER TUB AT DIFFERENT TIME POINTS

	Control Tub							Oil Tub						
Date	6-Feb	7-Feb				8-Feb	13-Feb	6-Feb	7-Feb				8-Feb	13-Feb
Time	4pm	3am	8am	11am	2pm	11am	10am	4pm	3am	8am	11am	2pm	11am	10am
I_d	w	a	c	d	e	f	g	W	A	C	D	E	F	G
N_{ss}	–	1	1	1	1	1	1	–	1	1	1	2	1	1
N_b	–	–	1	1	1	3	3	–	–	1	1	3	10	4
N_{sw}	1	–	–	–	–	1	1	1	–	–	–	–	1	–

I_d = sampling identification, N_{ss} = number of sampled sea ice surface, N_b = number of sampled bulk sea ice, and N_{sw} = number of sampled seawater.

around the inside perimeter of both tubs, and GPS coordinates were collected for each GCP to allow for geometric correction in UAV-generated digital elevation models (DEMs). Surface roughness parameters, such as σ_h and L_c, were calculated for UAV DEM elevations, following the expression in (5) and (6).

D. Scatterometer Methods

The radar backscatter measurements were obtained using a custom-designed C-band polarimetric scatterometer system (CSCAT), built by ProSensing Inc., USA. CSCAT is a solid-state frequency-modulated continuous-wave radar that functions with a central frequency of 5.5 GHz and a bandwidth of 500 MHz. With the aid of a dual-polarized parabolic antenna, it linearly transmits and receives radar pulses in quad-polarization modes: VV, VH, HV, and HH; thus, it provides a full backscattering matrix of objects under study. Inside the system, a positioning device is used to control the antenna to scan in elevation angles from 0°–80° and azimuth angular widths from 0°–340°. For measurement reliability and accuracy purposes, CSCAT is designed to automatically calibrate, internally with an attenuator and a 4.2-m-long delay line and externally with a trihedral corner reflector. A summarized specification of the CSCAT is given in Table II.

During the experiments, we mounted the CSCAT on a scaffolding platform at a height of 5.3-m relative to the seawater in both tubs (see Fig. 1). For 8-h, we continuously collected CSCAT measurements over the oil tub and then alternated backscatter collection between tubs, about every hour [46]. Using elevation angles of 12.5°–38.5° (in 2° steps) for the oil tub and 12.5°–36.5° for the control tub (in 2° steps), CSCAT continuously scanned both surfaces of the tub during the growth cycle of sea ice with an azimuth width of 10°. This azimuth width was selected to accommodate more independent samples while avoiding significant edge

TABLE II
CSCAT OPERATING SPECIFICATIONS

Centre frequency	5.5 GHz
Sweep bandwidth	500 MHz
Transmitted power	−6 dBm
Range resolution	30-cm
Antenna type	Parabolic reflector with dual polarized feed
Antenna Half-Power Beamwidth	5.7°
Cross-polarization isolation	>28-dB
Polarization modes	VV, VH, HV, HH
Calibration:	
External	Trihedral corner reflector
Internal	Attenuator and 4.2-m delay line

effect from each tub. The elevation angles were chosen to optimize data collection possibilities, and after postprocessing, we had to discard several high and low incidence angles due to the edge effects. The angles were verified using an angle finder (which is why the incidence angles are corrected to 0.5° accuracy and are not integer values, as in our previous experiments [17]–[19]). For each elevation scan, the returned power was averaged, and we calculated the NRCS from preoil injection to postoil migration ice in all polarization modes. To ensure data quality and control, we examined various scans on a pulse-by-pulse basis. We found that the average noise equivalent sigma zero (receiver noise floor) was -45 dBm^2/m^2 in the copolarization mode and -50 dBm^2/m^2 in the cross-polarization mode for all elevation angles. However, we opted to use 24.5° elevation angle data for our analysis because it was not affected by the tubs' edge effect. We used a five-point rolling mean filter to reduce the system noise and identify the overall trend of the data.

$$\frac{V_b}{V} = \left[\frac{(1\times 10^{-3}\mathrm{P}_i)S_b}{F_1(T_{\mathrm{si}}) - (1\times 10^{-3}\mathrm{P}_i)S_b F_2(T_{\mathrm{si}})}\right]\left[1 - \frac{V_a}{V}\right] \tag{2}$$

$$P_i = 917 - 0.1403T_{\mathrm{si}} \tag{3}$$

$$\left.\begin{aligned} F_1(T_{\mathrm{si}}) &= -4.732 - 22.45T_{\mathrm{si}} - 0.6397T_{\mathrm{si}}^2 - 0.01074T_{\mathrm{si}}^3 \\ F_2(T_{\mathrm{si}}) &= 0.08903 - 0.01763T_{\mathrm{si}} - 5.33\times 10^{-4}T_{\mathrm{si}}^2 - 8.801\times 10^{-6}T_{\mathrm{si}}^3 \end{aligned}\right\} -2 \geq T_{\mathrm{si}} \geq -22.9\ ^\circ\mathrm{C} \tag{4}$$

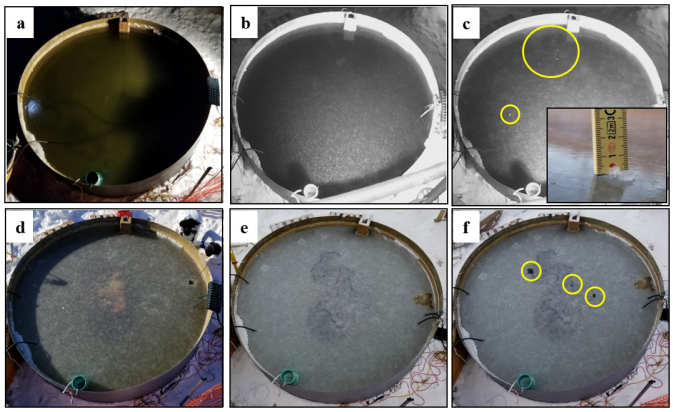

Fig. 3. Phase 1 progression of sea ice growth cycle in the oil tub: (a) February 7 at 00:00—calm open water after heater and pumps have been switched off, (b) 03:00 (third hour)—Frazil ice covering the ice surface, (c) 07:00 (seventh hour)—few sparsely distributed frost flowers, inset shows that the ice was <1-cm thick, (d) 13:00 (13th hour)—signs of oil migrating up through the middle area of the ice surface, immediately after oil injection, (e) February 8, 08:00 (32nd hour)—absorbed traces of snowfall on the surface, and (f) 10:30 (34.5th hour)—three spots of oil migrating onto the surface.

IV. Results

A. Physical Sampling Results

1) Phase-One Experiment Observation: The phase-one experiment (scenario in which oil was injected beneath a consolidated sea ice sheet) started at midnight on February 7, 2020, immediately after the heaters and pumps were switched off [see Fig. 3(a)]. Visible vapor flux rose steadily from the seawater surface in both the control and oil tubs. An hour later, we observed frazil ice nucleating from the open water, and it completely covered the seawater surface by the third hour [see Fig. 3(b)]. With a clear sky and very little wind, the atmospheric pressure was 101.4 kPa, the air temperature was −20 °C, and the surface temperature was −12 °C (see Fig. 4). At the third hour, we took our first bulk samples from each tub. The ice core was 1-cm thick, with surface salinities of 25.21 PSU in the control tub and 24.62 PSU in the oil tub (see Table III).

Between the fourth and eighth hours, the ice (dark nilas) thickened from 1.8 to 3.4 cm, with visible vapor flux from its surface. A Kimwipe test revealed that the ice surface had moisture accumulation, and we observed the formation of several frost flowers at the fifth hour. By the seventh hour, a few frost flowers (∼1% areal coverage) were sparsely distributed and short-lived, growing approximately 0.5-cm in height [see Fig. 3(c)]. The corresponding meteorological variables show that the atmospheric pressure remained close to 101.4 kPa, while both the air temperature and ice surface temperature decreased (see Fig. 4), resulting in a 7–13 °C temperature gradient and $T_s - T_a$ (difference between surface temperature T_s and air temperature T_a) [see Fig. 4]. As time elapsed, we collected our third bulk samples from each tub at the 11th hour (see Table III). By the 12th hour, the irradiance flux indicates that the sun (downwelling shortwave radiation, K_{down}) was 472 W/m^2 high and had begun to illuminate the surface (see Fig. 4).

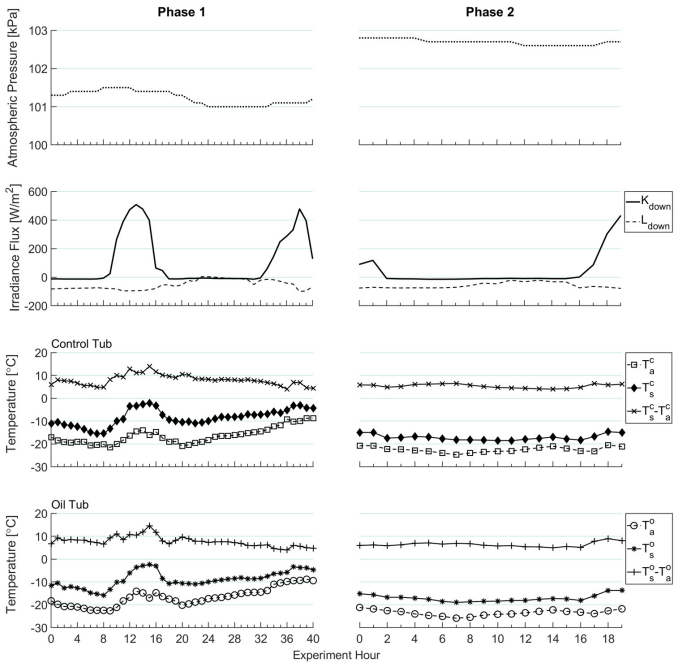

Fig. 4. Onsite meteorological conditions during phase 1 and 2 experiments. (From Top) Figures represent the following variables: atmospheric pressure, irradiance flux (downwelling shortwave K_{down} and downwelling longwave L_{down}), and temperature (air, T_a—10-cm above the ice surface; ice surface T_s; and their differences $T_s - T_a$). The top four figures were taken from a proxy meteorological station, while the bottom four were collected from the thermocouple strings inserted in both the control and oil tubs.

At the 12.5th hour, we performed the oil injection operation and introduced the oil into the tub, as described in Section III-A. The oil temperature was recorded at −8.7 °C. By the 13th hour, the oil was visible through the ice, which was 4-cm thick [see Fig. 3(d)]. We collected bulk samples at the 14th and 35th hours, and their physical properties revealed that the ice thickness had increased by ∼3-cm, as well as the presence of oil in the 35th hour ice core samples, which is represented as oil volume fraction (see Table III).

Prior to collecting our final bulk samples at the 35th hour, a light dusting of snowfall covered the ice surface at the 26th hour, and by the 32nd hour, the snow had been absorbed onto the ice surface in both tubs [see Fig. 3(e)]. With cloudy skies at the 34th hour, the ice surface was wet based on the Kimwipe test. We observed the few traces of snowflakes falling onto the ice surface, as well as the first spot where oil was migrating onto the ice surface. By 34.5-h, three oil spots were visible and continued to increase in number throughout the experiment [see Fig. 3(f)].

From the time oil was injected to the end of the experiment, the meteorological variables in Fig. 4 show that the atmospheric pressure gradually dropped from 101.5 to 101 kPa, where it stayed constant for 10-h before rising to 101.1 kPa. K_{down} peaked twice; the first peak was ∼508 W/m^2 at the 13th hour, and the second peak was ∼478 W/m^2 at the 38th hour. The remaining K_{down} was close to zero throughout the experiment. Both the air and ice surface temperatures followed a typical diurnal variation, with colder temperatures at night and warmer temperatures during the day. Eventually, air temperatures rose to −10 °C near the 36th hour, and

TABLE III
ICE PHYSICAL SAMPLING RESULTS DURING PHASE 1 EXPERIMENT

	Control Tub					Oil Tub				
h_s	3	8	11	14	35	3	8	11	14	35
I_d	a	c	d	e	f	A	C	D	E	F
I_{th} (cm)	1	3.4	4	5	8	1	3.4	4	5	7.5
S_{si} (PSU)	25.21	32.57	28.69	38.47	48.25	24.62	31.15	27.89	37.23	47.76
S_b (PSU)	–	20.61	19.89	18.65	16.28±1.04*	–	20.98	19.58	18.84±0.28*	13.05±1.35*
	–	–	–	–	18.41†	–	–	–	–	17.50±0.86†
T_{ss} (°C)	−11.95	−11.95	−11.22	−2.66	−7.93	−11.95	−12.94	−12.67	−3.99	−7.75
T_{si} (°C)	–	–	−4.66	−3.20	−6.35*	–	–	−3.18	−3.08	−5.14*
	–	–	–	–	−5.27†	–	–	–	–	−4.48†
V_o (%)	–	–	–	–	–	–	–	–	–	0.670±0.006*
	–	–	–	–	–	–	–	–	–	0.380±0.004†

h_s = sampling hour, I_d = sampling identification, I_{th} = sea ice thickness, S_{si} = Sea ice surface salinity, S_b = Sea ice bulk salinity T_{ss} = sea ice surface temperature, T_{si} = sea ice volume temperature, and V_o = oil volume fraction. Superscript '*' denotes top 5-cm ice section, and '†' denotes bottom 3-cm ice section in the control tub and 2.5-cm in the oil tub.

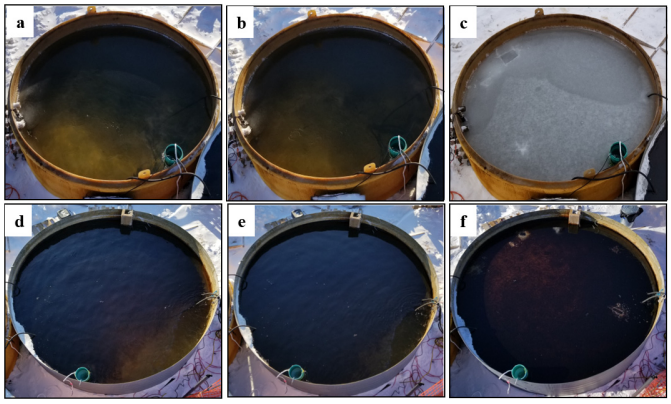

Fig. 5. Phase 2 progression of the sea ice growth cycle in (a)–(c) control and (d)–(f) oil tubs: on February 12, 16:00: calm open water after heater and pumps has been turned off (a—control tub and d—oil tub); February 12, 16:30: unchanged seawater surface in (b) control tub against a thin layer of skim oil (∼0.1-mm thick) covering the oil-contaminated seawater surface in (e) oil tub; and February 13, 11:30: light gray surface appearance of the ice in (c) control tub, against the dark surface appearance of the ice in (f) oil tub.

with this substantial change in temperature, we ended the phase-one experiment by performing comprehensive sampling of the contaminated sea ice.

2) Phase-Two Experiment Observation: For the phase-two experiment, we turned on heaters in both tubs to melt the existing sea ice formed in the first phase with the goal of evaluating sea ice formation when the water had previously been contaminated with crude oil. This experiment began at 16:00 on February 12, 2020, immediately after the heaters and pumps were turned off [see Fig. 5(a) and (d)]. Within 30 min, a thin layer of oil skim (∼0.1-mm thick) was found on the surface of the oil-contaminated seawater [see Fig. 5(b) and (e)]. Frazil ice began to develop on the surface of each tub after an hour. By the third hour, we noticed that the frazil ice in the oil tub was thinner (4-mm thick) than the one in the control tub (1-cm thick). The sky was clear, with a very low wind speed, an atmospheric pressure of 102.8 kPa, an air temperature of −23 °C, and an ice surface temperature of −17 °C [see Fig. 4 (left)]. For the rest of the experiment, the meteorological variables in Fig. 4 (left) show that the atmospheric pressure remained relatively stable at ∼102.7 kPa. K_{down} was close to zero, except for the early and late hours, when it peaked at ∼117 and ∼431 W/m^2, respectively. The air and ice surface temperatures remained cold and were approximately −23 °C and −17 °C, respectively [see Fig. 4 (left)].

TABLE IV
ICE PHYSICAL SAMPLING RESULTS DURING PHASE 2 EXPERIMENT

	Control Tub	Oil Tub
Thickness (cm)	7	5
Surface Salinity (PSU)	46.85	37.51
Bulk salinity (PSU)	18.75±0.69	15.95±0.16
Surface temperature (°C)	−14.5	−12.9
Volume temperature (°C)	−7.89	−6.68
Oil volume fraction (%)	None	2.98

The oil-contaminated ice grew without being sampled until 15-h later (February 13, 10:00), when we began collecting bulk samples [see Fig. 2 (bottom)]. Three ice core samples were collected from the control tub, while four ice core samples were collected from the oil-contaminated tub. The physical properties show that the ice thickness and surface salinity were 2-cm and 20% lower, respectively, in the oil-contaminated tub than in the control tub (see Table IV). During the bulk sampling, we observed that the surface appearance of both tubs can be easily differentiated [see Fig. 5(c) and (f)]. The ice surface in the control tub appears light gray and visually rougher, while the ice surface in the oil tub appears dark and visually smoother.

B. LiDAR and UAV Results

Two sets of LiDAR measurements were carried out in each tub at the 9.5th (February 7, 9:30) and 13.5th (February 7,

TABLE V
SURFACE ROUGHNESS PARAMETERS DURING PHASE 1 EXPERIMENT

		Control Tub		Oil Tub	
Date	Hour	σ_h(cm)	L_c(cm)	σ_h(cm)	L_c(cm)
Feb. 7, 9:30	9.5	0.489	0.990	0.411	1.047
Feb. 7, 13:30	13.5	0.440	0.957	0.447	0.901
Feb. 7, 17:00	17.0	0.509*	–	0.396*	–
Feb. 8, 11:30	35.5	0.143*	–	0.194*	–

The parameters σ_h and L_c denote the rms-height, and correlation length. The standard deviation of L_c is 0.002-cm Superscript '*' represents measurements collected with UAV, while the rest were collected with LiDAR.

13:30) hours, to characterize the ice surface variations before and immediately after the oil injection. In the oil tub, the rms height σ_h for the first measurement is 0.411-cm, and the average correlation length L_c is 1.047-cm. Meanwhile, in the control tub, $\sigma_h = 0.489$-cm and $L_c = 0.990$-cm. Refer to Table V for the 13.5th hour parameters.

At the 17th (February 7, 17:00) and 35.5th hours (February 8, 11:30), two sets of UAV measurements were acquired in each tub. As shown in Table V, σ_h decreased from 0.396 to 0.194 cm in the oil tub and from 0.509 to 0.143 cm in the control tub. Throughout the LiDAR and UAV measurements, the ice surface was bare except for the 35.5th hour when the ice surface had absorbed the accumulation of trace snowfall.

C. Scatterometer Results

1) Temporal Observation of Phase-One NRCS: Fig. 6 shows the time series response of C-band multipolarization NRCS measured during the phase-one experiment, at an incidence angle of 24.5°. Generally, in the oil tub, the NRCS shows that the copolarized responses—VV and HH—are closely related during the initial stage of sea ice formation, but their gap widens to about 2-dB under steady sea ice growth and calm conditions. The cross-polarized responses—VH and HV—are lower than the copolarized NRCS in the order of 2–21 dB. Fig. 6 depicts only the VH return because our scatterometer device is configured in a monostatic mode; hence, the assumption of reciprocity is established between VH and HV. It should be noted that two local maxima were observed during the measurement; the first occurred around the sixth hour, prior to oil injection, and the second occurred around the 34th hour, long after oil injection.

To evaluate the relative behavior of the NRCS from the oil tub, we considered the NRCS from the control tub as a proxy, as shown in Fig. 6 (right). There were physical and scattering differences between the two tubs as the volume differences result in differences in the ice rate of growth. The oil tub's measurement begins with a very low backscatter return (VV = −43 dB, HH = −44 dB, and VH = −50 dB), which is close to the receiver noise floor of the scatterometer system (refer to Section III-D), and within 4-h, a stable NRCS for all polarizations was observed. Between the fourth and eighth hours, an abrupt transient increase in the 25-dB range is observed in the multipolarization NRCS (from −40 to −19 dB for VV, −42 to −16 dB for HH, and −46 to −30 dB for VH), followed by a return to a steady-state level (VV = −34 dB, HH = −38 dB, and VH = −46 dB), as the ice developed from calm open water to about 2-cm-thick dark nilas. By the 12th hour, the dark nilas had grown to 4-cm thick, the VV remained relatively flat at −32 dB, the HH slightly rose from −36 to −35 dB, and the VH slightly dropped from −44 to −45 dB.

Following the oil injection at the 13th hour, the NRCS for VV and HH trended 3-dB upward (between the 13th and 22nd hours) and downward (between the 22nd and 30th hours). The upward trend values for VV range from −32 to −29 dB while for HH range from −34 to −31 dB. Both VV and HH have the opposite downward trend values (with a small bump between the 22nd and 30th hours). In the case of VH-polarization, we observed that the NRCS stayed constant at approximately −46 dB for ∼5-h before rising by 9-dB (from −46 to −37 dB) stabilizing again between the 22nd and 30th hours, at around −37 dB.

Close to the 32nd hour, before we observed the initial oil migrating onto the ice surface at the 34th hour, our scatterometer observations showed a local minimum, followed by an increase of ∼13 dB for copolarized signals (from −36 to −23 dB for VV and from −37 to −26 dB for HH) and a coincident decrease of ∼9 dB in the cross-polarized signal (from −36 to −45 dB). Between the 34th and final hours of the experiment, as the oil spread on the surface, the copolarized signals fell to about −33 dB for VV and −36 dB for HH, while the cross-polarized signal level was near −45 dB with a minor peak at −40 dB.

The control tub measurements began at the eighth hour of the experiment, as we had to alternate look angles of the scatterometer to monitor each individual tub and chose to focus on the oil tub during the initial freeze-up [see Fig. 6 (right)]. The copolarized signatures are almost aligned and exhibit an upward trend by 8-dB (from −35 to −26 dB) toward the end of the experiment. Between the 30th and 32nd hours, an increase of 6-dB was observed in the copolarized signals. This increase was a transient event that lasted for 2-h, and by the 34th hour, the copolarized signals reached a steady state at −27 dB. Meanwhile, the VH return was relatively constant throughout the experiment, at approximately −43 dB, with the exception of a few transient signals between the 30th and 34th hours.

2) Temporal Observation of Phase-Two NRCS: Fig. 7 shows the time series response of C-band multipolarization NRCS, during the phase-two experiment, at an incidence angle of 24.5°. It should be noted that only NRCS data from the oil tub were acquired. With the exception of a few greater backscatter levels in the first hour of measurement, throughout the experiment, the multipolarization NRCS response remained relatively stable at approximately −39 dB for VV, −42 dB for HH, and −46 dB for VH.

V. DISCUSSION

The main objective of this research was to establish how the physical and thermodynamic properties of oil-contaminated newly forming sea ice impact C-band backscatter and to evaluate how these results can be used to remotely detect oil in

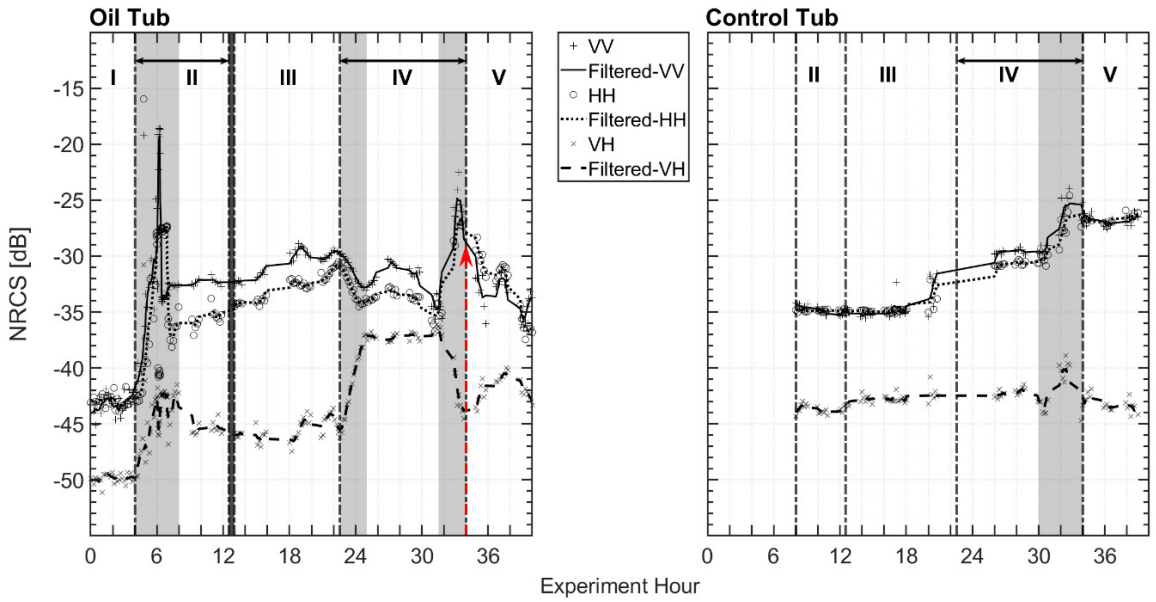

Fig. 6. Temporal multipolarization NRCS measured during the phase-one experiment at an incidence angle of 24.5°. The markers represent the raw measured data, whereas the lines represent the best fit lines of the raw multipolarization NRCS measurements to reveal the underlying time-series patterns. The black vertical thick line illustrates the period (between 12.5th and 13th hours) when oil was injected beneath the sea ice, and the red vertical arrow line shows the period (about the 34th hour) when the initial oil migrated onto the ice surface. Based on the sampled ice thickness in Table III, as well as when oil was injected beneath the ice sheet, and when oil migrated onto the ice surface, the C-band multipolarization NRCS in the oil tub were characterized into five ice regimes (I–V): frazil, dark nilas, oil-contaminated dark nilas without surface oil migration, oil-contaminated light nilas without surface oil migration, and oil-contaminated light nilas with surface oil migration, respectively. Meanwhile, in the control tub, Regimes II and III represent dark nilas, and Regimes IV and V represent light nilas, based on the sampled ice thickness in Table III. The light-gray shaded areas represent the transition period between regimes.

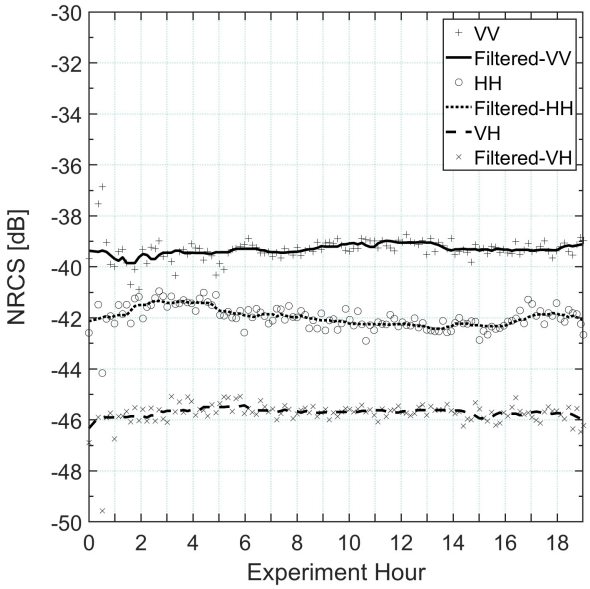

Fig. 7. Temporal multipolarization NRCS measured in the oil-contaminated tub, during the phase-two experiment, at an incidence angle of 24.5°. The markers represent the raw measured data whereas, the lines represent the best-fit lines of the raw multipolarization NRCS measurements to reveal the underlying time-series patterns.

newly forming sea ice. We used the phase-one scatterometer results in Fig. 6 (left) to characterize the sea ice growth cycle into five distinct regimes: 1) frazil; 2) dark nilas; 3) oil-contaminated dark nilas without surface oil migration; 4) oil-contaminated light nilas without surface oil migration; and 5) oil-contaminated light nilas with surface oil migration. On this basis, we will discuss our interpretations of the results presented in Section IV. We used the term "surface oil migration" to refer to the visual observation of oil migrating up through the ice surface. Regarding the phase-two experiment, the discussion will be guided by the scatterometer data (see Fig. 7) and physical sampling results (see Table IV).

A. Phase-One Experiment

The goal of the phase-one experiment was to understand the multipolarized backscattering characteristics of the oil-contaminated NI and relate them to the geophysical and thermodynamic nature of the oil in sea ice. To answer the first research question in Section I: "what are the relationships between the physical, thermodynamic, and microwave C-band scattering properties of newly-forming sea ice in our mesocosm leading up to and following an oil spill event?"

1) Regime I—Frazil: As expected, the initial ice (frazil) that forms from calm open water has extremely low multipolarization NRCS responses [see Fig. 6 (left)]. This is due to low wind conditions resulting in a smooth surface, causing it to act as a specular scatterer for any incoming radar signal, thereby weakening the multipolarization NRCS responses. Moreover, once the frazil ice completely covered the seawater surface [see Fig. 3(b)], we observed that multipolarization NRCS responses remained unchanged. This could be attributed to the smoothness of the ice surface, which also acts as a specular scatterer [20]. Similar temporal NRCS behavior was observed in [18] and [36] for C-band scatterometer measurements of NI during its initial growth.

2) Regime II—Dark Nilas: Within this regime, the scatterometer measured a local maximum at all polarization [see Fig. 6 (left)]. The peaks for VV, HH, and VH were −19, −16,

and −30 dB, respectively. This is a transient behavior related to a rapid surface brine expulsion, which facilitates frost flower formation [47] and, thus, increases the surface dielectrics. Surprisingly, only a few (∼1% area coverage) sparsely distributed and short-lived (0.5-cm growth height) frost flowers were observed [see Fig. 3(c)] even though the conditions for its growth were apparently optimal: brine-wetted surface, positive temperature gradient, and very little wind. We did not measure relative humidity near the surface. The few sparse distributions suggest that the surface was very smooth, resulting in a limited number of nodule sites (protrusions through the overlying brine-wetted layer) for frost flower nucleation [48]. The short-lived growth of frost flowers could be attributed to a shallow temperature gradient between the sea ice surface and the air. The previous study [36] showed that a steep temperature gradient (>12 °C) contributes to the favorable atmospheric conditions that sustain the growth of frost flowers. Other studies in [38], [49], and [50] demonstrated that the frost flowers deteriorate as the temperature gradient drops (<12 °C). Ours was below 10 °C, indicating that the temperature gradient was insufficient.

The core sample at the 11th hour revealed that the ice had thickened to 4 cm, and the surface salinity had decreased by ∼3 PSU [from 31.15 to 27.89 PSU (see Table III)]. This indicates that the ice growth rate has reduced after the surface brine expulsion.

Following the collapse of the local maximum, the NRCS did not revert to its previous level during the initial ice formation. This was expected, based on previous experiments on newly forming sea ice under cold conditions [36], [38]. Prior to the oil injection between hours 8 and 12, in the oil-contaminated tub, the VV remained nearly flat with a 2 dB increase over HH, which gradually trended upward, while the coincidental VH gradually trended downward [see Fig. 6 (left)]. In the control tub, however, no difference in NRCS was observed for the VV and HH polarizations, both of which had a nearly flat trend, as well as the corresponding VH polarization [see Fig. 6 (right)]. A slow growth rate may have contributed to the NRCS's flatness and gradual trending response. In addition, the NRCS responses in the control tub were consistent with the 25° incidence angle copolarized NRCS in [36]. However, in the oil tub, the NRCS responses were inconsistent with a 2-dB differential. We initially speculated that the NRCS differences were attributable to the uninsulated design of the oil tub versus the fiberglass insulated control tub (see Section III-A), but our core samples showed no substantial variation in the physical sampling results (see Table III). This is the first time that the authors used the control tub in close proximity to their main experiment, and the comparison revealed a high degree of NRCS variability in NI types, even under similar environmental conditions [34]. Although the microstructure of NI types was not analyzed during our experiment, visual observation of ice core samples revealed granular structure, which aligns with nilas [42], [51]. In future experiments, we will conduct ice microstructure analysis to address this shortcoming.

3) Regime III—Oil-Contaminated Dark Nilas Without Surface Oil Migration: Within this regime, the dark nilas was contaminated as a result of oil injection between the 12.5th and 13th hours [see Fig. 6 (left)]. We visually observed the oil migrating toward the middle of the ice surface [see Fig. 3(d)] due to its thinness (4-cm thick); however, none of the oil was able to migrate up through to the surface. The oil that migrated toward the middle of the surface indicates that the oil spreads unevenly, with the majority concentrated in the center of the tub at the ice–water interface. This is supported by our bulk samples (E1–E3) at the 14th hour [see Fig. 2 (top left)], which revealed oil staining only at the bottom tip of the samples.

Two mechanisms could account for the absence of instantaneous oil migration to the surface: a small oil volume fraction [32], [33] and interspersed granular brine pockets [30]. The volume of oil migrating toward the surface was small relative to the brine volume in the topmost layer of the dark nilas. According to studies by Desmond *et al.* [32] and Saltymakova *et al.* [33], brine pockets require ≥2% of oil volume fraction (within the top 5-cm) to be displaced during upward migration. This is consistent with our previous experiment [18], in which 20-L of crude oil was used to achieve an 8.4% oil volume fraction and observed instantaneous oil migration to the surface. The authors acknowledge that we lacked the data needed to validate the results in [18] because no sample was taken in the center of the tub as the necessary destructive sampling would have interfered with the radar scan footprint. With regard to the second explanation, the topmost layer of new sea ice is characterized by interspersed granular brine pockets that act as a barrier to oil migration [30], resulting in the oil becoming encapsulated as the ice sheet grows [28]–[30].

The corresponding NRCS showed that both VV and HH slightly increased by 3-dB, while VH remained relatively constant and gradually increased by 1-dB at the end of this regime [see Fig. 6 (left)]. This means that the NRCS within the C-band frequency range did not immediately respond to oil beneath the sea ice [52]. However, the increasing trend has shown that C-band NRCS is responsive to new sea ice thickening under constant growth and calm conditions. This is supported by the progression of our physical sampling data (from both oil and control tubs) [see Fig. 4 and Table III]. As our LiDAR measurements show no measurable differences in the rms height and correlation length (see Table V), we are drawn to conclude that the increase in the backscatter was driven by an increase in the dielectric constant. This is confirmed by our physical sampling data, which depicts increasing surface salinity as the ambient temperature rises (see Fig. 4 and Table III).

4) Regime IV—Oil-Contaminated Light Nilas Without Surface Oil Migration: Within this regime, the oil-contaminated dark nilas had transformed into light nilas with no evidence of surface oil migration. This was based on visual observations of the ice surface, while bulk samples were not collected to substantiate our claim; we do know that the ice had grown to a thickness of 5-cm during the previous regime. With sustained cold air temperature, we anticipated that this regime will be thicker than 5-cm, which is characteristic of light nilas.

Our scatterometer measurements showed that the NRCS for the copolarized signals slightly decreased by 3-dB and remained constant with a minor change in response for 5-h [see Fig. 6 (left)]. Meanwhile, the VH increased by 7-dB before plateauing for 5-h. The corresponding NRCS in the control tub showed that the copolarized signals gradually increased, while the VH leveled off [see Fig. 6 (right)]. We expected an increasing copolarized response [as seen in Fig. 6 (right)] because the ambient temperature was rising [20] [see Fig. 4 (last figure from top)], which is often associated with increasing brine volume [37]. The unexpected decreasing trend in the oil tub suggests that the encapsulated oil was impeding the upward movement of the brine of its underlying ice sheet, causing a brine rejection into the seawater column [28], [29]. This phenomenon decreases the sea ice surface dielectrics, thereby weakening the NRCS [37]. Simultaneously, the encapsulated oil may have introduced some inhomogeneity into the upper layer of ice volume, resulting in a coincidental increase of VH. Cross-polarized signals, such as VH, are frequently enhanced by multiple or volume scattering of an inhomogeneous medium, such as oil-contaminated sea ice [37]. In the case of the minor change in response to the copolarized NRCS, it could be attributed to the trace snowfall that began at the 26th hour. The fact that that VH remained stable during the trace snowfall means that the copolarized signals (VV and HH) were more responsive.

Close to the 32nd hour, 2-h before Regime V, we observed a clear trend change such that the copolarized signals began to trend upward while the corresponding cross-polarized signal trended downward [see Fig. 6 (left)]. This is related to the onset of upward brine migration, which was triggered by the upward movement of the oil that had been encapsulated within the ice sheet for 18.5-h. We speculate that the upward movement of the encapsulated oil was permitted by the warming ambient temperature [28]–[30] [see Fig. 4 (last figure from top)]. This combined brine and oil migration, similar to the brine expulsion event in Regime II, change the ice surface dielectrics, thereby enhancing the copolarized signatures. In contrast to the brine expulsion event in Regime II, the cross-polarized signal (VH) exhibited a downward trend. The VH showed a downward trend because of the combined upward migration of brine and oil, which prevents microwave penetration into the sea ice sheet, where multiple and volume scattering from inclusions would give rise to a cross-polarized backscatter signal. Notably, in the control tub, we observed an increase in backscatter around the same time, which we attributed to changes in the thermodynamic state of the sea ice that was warming due to incoming solar radiation. The distinct differences in backscatter level change in the oil tub (an increase of 13-dB for copolarized signals and decrease of 9-dB for the cross-polarized signal) versus the control tub (increase of 6-dB for copolarized signals and increase of 5-dB for the cross-polarized signal) can be used to segment regions of sea ice with and without oil contamination.

From these results, we speculate that the emergence of oil at the surface of the sea ice could be tracked through a combination of copolarized and cross-polarized signal time-series analyses. The transient increase of copolarized backscatter indicates an upward flux of brine toward the surface of the sea ice. This is not a unique result, however, as seen by our experimental data. When brine is rejected toward the surface in early ice growth, we can expect to observe an increase in cross-polarized backscatter. In contrast, suppose we know that an ice sheet has been established through time-series measurements. If we observe a similar transient increase of copolarized signals, coupled with a transient decrease in cross-polarized signals, then further investigation is merited, as this has been shown to be linked to oil presence in sea ice. We suggest that additional analysis and experimentation should be performed to understand the applicability and limitations of these results.

5) Regime V—Oil-Contaminated Light Nilas With Surface Oil Migration: We identified the beginning of Regime V with the initial observations of oil migrating onto the sea ice surface [see Fig. 6 (left)]. At the beginning of Regime V, the copolarized signals VV and HH were equal and exhibited a decrease of approximately 6- and 9-dB for VV and HH, respectively. Notably, between the 34th and 39th hours, the HH signal is greater than VV; however, from the 39th hour to the end of the experiment, VV is greater than HH. The cross-polarized signal starts at -43 dB, shows a small increase of 2-dB, and then returns to -43 dB at the end of the experiment.

Examination of the core samples revealed that the surface salinity had increased by 22% relative to Regime III [from 37.23 to 47.76 PSU (see Fig. 5)], meaning that the upward oil movement was promoting surface brine migration. Although the oil volume fraction within the top 5-cm ($\sim$0.7%) is less than the required 2% claimed by Desmond *et al.* [32] and Saltymakova *et al.* [33], the upward movement of oil via the conduits of brine channels accelerates as the ambient sea ice temperature increases [28]–[30], displacing brine onto the ice surface. This indicates that the lower the oil volume fraction ($<$2%), the longer it takes for the oil to migrate onto the ice surface, under stable freezing temperatures. We hypothesize that this finding is unique in which the C-band has the potential to be sensitive to minor oil spills; however, future experiments are needed to test the robustness of this result.

Regarding the dramatic drop of VH, we speculated earlier in Regime IV that it was probably caused by the combined upward migration of brine and oil, which prevents microwave penetration into the sea ice volume. Fortunately, in this regime, we have core samples to relate with. The bulk salinity depicts that the top-5-cm section was 31% (13.05 PSU) lower than Regime III (18.84 PSU), and no measurable differences were found in the bottom ice section (see Table III). Moreover, the surface salinity is greater in Regime V (47.76 versus 37.23 PSU). These data agree with our suggestion that the brine is expelled toward the surface as the oil propagates upward.

Following the initial oil migration onto the ice surface, a significant drop was observed for both the VV and HH. The corresponding VH, on the other hand, stayed relatively stable with a minor peak. This indicates that the copolarized NRCS was immediately responsive to the presence of the oil on the ice surface, and the downward trend continued as the oil migrated onto the surface. Because oil has a lower dielectric

constant compared to a highly saline, brine-wetted sea ice surface, the decrease in backscatter is generally expected; however, the relationship is complex, as there is a mix of brine and oil on the surface. Further studies on the properties of brine/oil mixtures on the top of sea ice would be helpful to understand this complex interaction. In comparison, the copolarized signatures in the control tub are almost aligned and exhibited an upward trend, while the VH return was relatively constant throughout the experiment [see Fig. 6 (right)]. This is similar to our earlier findings in Regime II, where the VV and HH in the oil tub were more responsive to growing sea ice than the VH. However, when the oil migrated up through the ice surface of the oil tub [see Fig. 6 (left)], the VV and HH signatures changed course and began to trend downward, in contrast to the increasing trend in the control tub. This confirms our expectation that oil on the ice surface reduces the NRCS response, specifically the copolarized signatures.

The final set of UAV measurements conducted at the 35.5th hour (see Table V) provides additional support to our findings. Compared to Regime III, the rms height in the oil tub was reduced by 51% (from 0.396 to 0.194 cm) and in the control tub by 72% (from 0.509 to 0.143 cm). We attributed these rms-height reductions to the wetness of the ice surface, which is caused by the presence of oil (only in the oil tub), absorbed traces of snowfall, and incoming solar radiation [see Fig. 4 (second figure from top)]. As seen in Table V, we did not report the correlation lengths for the UAV dataset because they were physically meaningless. The correlation lengths were overestimated by a factor of 20, which is significantly higher than the reported values in the literature (e.g., [18], [25], and [38]). Because of its low spatial resolution, caution should be taken in using UAV-measured surface roughness parameters, as it could lead to a misinterpretation of the physical meaning. However, we advised that UAV can be used as a complement to LiDAR measurements of surface roughness. Future work on small-scale surface roughness measurements could use both LiDAR and UAV systems contemporaneously to determine the intercomparability between instrument measurements and evaluated parameters.

B. Phase-Two Experiment

The Phase 2 experiment focused on the growth of sea ice from seawater with an oil slick on the surface. To answer the second research question in Section I: "how does the presence of a layer of oil on seawater influence the growth, physical properties, and microwave C-band scattering properties of newly-forming sea ice?"

Physical sampling and scatterometer results are presented in Table IV and Fig. 7, respectively. Core samples revealed that the ice in the oil tub had grown to 5-cm thick, while the ice in the control tub had grown to 7-cm thick. This demonstrates that the ice in the oil tub grew in the midst of oil-contaminated seawater, and it agrees with the conclusion of [53] that oil-contaminated seawater does not prevent ice growth. However, it has been proposed that the insulating properties of oil may slow the rate of ice growth beneath the oil skim [31], [32]. As shown in Table IV, the surface salinity in the oil tub (37.51 PSU) was 20% lower than that of the control tub (46.85 PSU). The surface layer of the ice in the oil tub had a high oil volume fraction ($\sim$3%), resulting in a warmer sea ice surface, which could account for the 20% lower salinity in the oil tub than the control tub [32] and [33]. It should be noted that we encountered difficulties scraping the oil-covered ice surface because the ice immediately became infiltrated with the surrounding oil. Although new techniques need to be established to hold back the oil during data collection in the future, we were successfully able to extract the topmost layer (0.5-cm thick) of the sea ice.

Throughout the experiment, the NRCS results (oil tub) were flat (see Fig. 7). This is in contrast to the results in Phase 1, where the backscatter exhibited a large increase ($>$25-dB) with the growth of sea ice. Compared to the control tub of phase one, it is clear that C-band NRCS can potentially distinguish between uncontaminated and oil-contaminated new sea ice, provided that the oil spill is on the ice surface. Another important finding is that the presence of oil on the surface of Arctic waters could mask the underlying sea ice growth, which has implications for marine transportation and safety. Fig. 5(f) supports our claim, as the oil layer clearly obscured the ice sheet below, which responded to the near-constant NRCS seen in Fig. 7.

VI. Conclusion

This article has explained the results of two different scenarios of multipolarization C-band scatterometer experiments performed on oil-contaminated NI. In phase one, oil was injected beneath a consolidated ice sheet, and in phase two, ice was grown in oil-contaminated simulated Arctic seawater.

For phase one, we assessed the time-series evolution of multipolarization C-band scatterometer measurements in relation to the physical and thermodynamic properties of oil-contaminated sea ice. These relationships resulted in the characterization of five distinct ice regimes [see Fig. 6 (left)]: 1) frazil; 2) dark nilas; 3) oil-contaminated dark nilas without surface oil migration; 4) oil-contaminated light nilas without surface oil migration; and 5) oil-contaminated light nilas with surface oil migration. We used the term "surface oil migration" to describe the visual observation of oil migrating up through to the ice surface. The initial ice (frazil) grew from calm open water through uncontaminated dark nilas to oil-contaminated light nilas with surface oil migration. Throughout the experiment, two local scattering maxima were observed [see Fig. 6 (left)]. The first maximum occurred at the onset of Regime II and was associated with a rapid surface brine expulsion, which initiated the formation of frost flowers [47]. Despite favorable atmospheric conditions and a brine-wetted surface, we found only a few frost flowers ($\sim$1% areal coverage) that were sparsely distributed and short-lived with a growth height of 0.5-cm [see Fig. 3(c)]. The sparse distribution indicated the presence of a limited number of frost flower nucleation sites [48], while the short-lived growth of frost flowers, we attribute to a shallow temperature gradient between the sea ice surface and the air. The second maximum occurred near the end of Regime IV and was linked to a combined upward migration of brine and oil. The brine migration was triggered

by the upward movement of the oil that had been encapsulated within the ice sheet for 18.5-h due to an increasing trend in ambient temperature [28]–[30] [see Fig. 4 (last figure from top)]. Copolarized signals increased by 13-dB in response to the second maximum, while the corresponding cross-polarized signal decreased by 9-dB [see Fig. 6 (left)]. Once the first oil migrated onto the surface, the copolarized signals dropped dramatically, while the cross-polarized signal remained nearly constant with a minor bump. Following the oil injection, no oil was immediately observed on the sea ice surface. We proposed two possible explanations for the absence of instantaneous oil migration to the surface: a small oil volume fraction ($<2\%$) that was unable to displace the overlying brine pockets [32], [33] and interspersing granular brine pockets within the topmost layer that restrained the upward movement of oil [30]. The results of this experiment suggest that a combination of time-series copolarized and cross-polarized C-band backscatter data can be used to detect oil migration onto the sea ice surface.

We utilized a LiDAR sensor and UAV-based optical imagery to characterize the surface roughness of the ice sheet. The LiDAR showed no measurable difference between before and immediately after oil injection. The UAV data confirmed that the ice surface was relatively smoother as a result of oil surface migration, absorbed traces of snowfall, and incoming solar radiation. Because of its low spatial resolution, caution should be taken in using UAV-measured surface roughness parameters, as it could lead to a misinterpretation of the physical meaning. Nonetheless, we advise that the UAV could be used to complement LiDAR measurements. For comparison purposes, future work may consider small-scale surface roughness characterization with both LiDAR and UAV systems contemporaneously.

Regarding the phase-two experiment, the goal was to examine the effect of oil-contaminated seawater on the growth of NI and the microwave backscatter. These datasets are rare, difficult to obtain, and can be used in modeling studies for the detection of oil in Arctic marine environments. The backscatter was relatively constant, even with the growth of sea ice. This is in contrast with the growth of sea ice when there is no oil present. In addition, a 3% oil volume fraction in the ice surface layer reduced the surface salinity by 20% compared to the uncontaminated ice surface [32] and [33].

Overall, the findings of this study have improved our understanding of oil scattering behavior, which can be used to detect oil spills in the Arctic marine environment. For instance, we were able to differentiate between brine expulsion and oil migration to the surface using low incidence angles (in our case, 24.5°), as well as a combination of copolarized and cross-polarized signatures. These parameters could serve as a baseline data interpretation for oil detection in the Arctic Ocean using current and future C-band multipolarization radar satellites. Our results show that the C-band backscatter is sensitive to Arctic oil spill events during freeze-up periods, as the thermodynamic state of sea ice influences upward oil migration. Future work will analyze the covariance and Mueller scattering matrices from this experiment to derive relevant polarimetric parameters that can discriminate between oil contaminated and uncontaminated NI.

ACKNOWLEDGMENT

The authors would like to thank Dave Binne [SERF Technician, Centre for Earth Observation Science (CEOS)] and Katarzyna Polcwiartek (Ph.D. Student, CEOS).

REFERENCES

[1] J. Dawson, L. Pizzolato, S. E. L. Howell, L. Copland, and M. E. Johnston, "Temporal and spatial patterns of ship traffic in the Canadian Arctic from 1990 to 2015," *Arctic*, vol. 71, no. 1, pp. 15–26, 2018, doi: 10.14430/arctic4698.

[2] A. K. Y. Ng, J. Andrews, D. Babb, Y. Lin, and A. Becker, "Implications of climate change for shipping: Opening the Arctic seas," *Wiley Interdiscipl. Rev., Climate Change*, vol. 9, no. 2, p. e507, 2018, doi: 10.1002/wcc.507.

[3] B. M. Boylan and D. Elsberry. (2019). *Climate Change and Maritime Traffic in the Arctic*. The Center for Arctic Policy Studies. Accessed: Oct. 2, 2021. [Online]. Available: https://uaf.edu/caps/our-work/policy-perspectives-files/climate-change-and-maritime-traffic-in-the-arctic-pb4-final-12dec2019.pdf

[4] M. Afenyo, B. Veitch, and F. Khan, "A state-of-the-art review of fate and transport of oil spills in open and ice-covered water," *Ocean Eng.*, vol. 119, pp. 233–248, Jun. 2016, doi: 10.1016/j.oceaneng.2015.10.014.

[5] National Energy Board. (2011). *Review of Offshore Drilling in the Canadian Arctic: Preparing for the Future*. Accessed: Feb. 15, 2021. [Online]. Available: https://www.cer-rec.gc.ca/en/about/north-offshore/arctic-offshore-drilling-review/2011-final-report/2011fnlrprt-eng.pdf

[6] T. Puestow. (2013). *Oil Spill Detection and Mapping in Low Visibility and Ice: Surface Remote Sensing*. Accessed: Feb. 26, 2021. [Online]. Available: http://www.arcticresponsetechnology.org/wp-content/uploads/2017/09/Report-5.1-SURFACE-REMOTE-SENSING.pdf

[7] *Responding to Oil Spills in the U.S. Arctic Marine Environment*, Nat. Academies Press, Washington, DC, USA, 2014.

[8] ITOPF. (2018). *ITOPF Arctic and Cold Climates: Detecting & Tracking Oil in Ice*. Accessed: Mar. 2, 2020. [Online]. Available: https://www.itopf.org/knowledge-resources/documents-guides/arctic-cold-climates/detecting-tracking-oil-in-ice/

[9] C. Brekke and A. H. S. Solberg, "Oil spill detection by satellite remote sensing," *Remote Sens. Environ.*, vol. 95, no. 1, pp. 1–13, Mar. 2005, doi: 10.1016/j.rse.2004.11.015.

[10] A. H. S. Solberg, "Remote sensing of ocean oil-spill pollution," *Proc. IEEE*, vol. 100, no. 10, pp. 2931–2945, Oct. 2012, doi: 10.1109/JPROC.2012.2196250.

[11] I. Leifer *et al.*, "State of the art satellite and airborne marine oil spill remote sensing: Application to the BP *Deepwater Horizon* oil spill," *Remote Sens. Environ.*, vol. 124, pp. 185–209, Sep. 2012, doi: 10.1016/j.rse.2012.03.024.

[12] M. Fingas, "Oil spill remote sensing," in *Oil Spill Science and Technology*, 2nd ed. Houston, TX, USA: Gulf, 2017, pp. 306–360.

[13] C. Brekke, B. Holt, C. Jones, and S. Skrunes, "Discrimination of oil spills from newly formed sea ice by synthetic aperture radar," *Remote Sens. Environ.*, vol. 145, pp. 1–14, Apr. 2014, doi: 10.1016/j.rse.2014.01.015.

[14] A. M. Johansson, C. Brekke, and G. Spreen, "Multi-frequency polarimetric SAR signatures of lead sea ice and oil spills," in *Proc. IEEE Int. Geosci. Remote Sens. Symp.*, Jul. 2017, pp. 1872–1875, doi: 10.1109/IGARSS.2017.8127342.

[15] M. Myrnes, C. Brekke, L. Ferro-Famil, and C. Petrich, "Polarimetric analysis of oil contaminated laboratory grown saltwater ice imaged by a ground based SAR," in *Proc. Eur. Conf. Synth. Aperture Radar*, 2018, pp. 1–4.

[16] A. M. Johansson, M. M. Espeseth, C. Brekke, and B. Holt, "Can mineral oil slicks be distinguished from newly formed sea ice using synthetic aperture radar?" *IEEE J. Sel. Topics Appl. Earth Observ. Remote Sens.*, vol. 13, pp. 4996–5010, 2020, doi: 10.1109/JSTARS.2020.3017278.

[17] N. Firoozy *et al.*, "An electromagnetic detection case study on crude oil injection in a young sea ice environment," *IEEE Trans. Geosci. Remote Sens.*, vol. 55, no. 8, pp. 4465–4475, Aug. 2017, doi: 10.1109/TGRS.2017.2692734.

[18] N. Firoozy *et al.*, "A controlled experiment on oil release beneath thin sea ice and its electromagnetic detection," *IEEE Trans. Geosci. Remote Sens.*, vol. 56, no. 8, pp. 4406–4419, Aug. 2018, doi: 10.1109/TGRS.2018.2818717.

[19] T. D. Neusitzer *et al.*, "Examining the impact of a crude oil spill on the permittivity profile and normalized radar cross section of young sea ice," *IEEE Trans. Geosci. Remote Sens.*, vol. 56, no. 2, pp. 921–936, Feb. 2018, doi: 10.1109/TGRS.2017.2756843.

[20] R. G. Onstott, "SAR and scatterometer signatures of sea ice," in *Microwave Remote Sensing of Sea Ice*, F. D. Carsey, Ed. Washington, DC, USA: American Geophysical Union, 1992, pp. 73–104.

[21] W. B. Tucker, D. K. Perovich, A. J. Gow, W. F. Weeks, and M. R. Drinkwater, "Physical properties of sea ice relevant to remote sensing," in *Microwave Remote Sensing of Sea Ice*, F. D. Carsey, Ed. Washington, DC, USA: American Geophysical Union, 1992, pp. 9–28.

[22] D. Isleifson, A. S. Komarov, D. Desmond, G. Stern, and D. Barber, "Modeling backscatter from oil-contaminated sea ice using a multi-layered scattering model," in *Proc. IEEE Int. Geosci. Remote Sens. Symp.*, Sep. 2020, pp. 3031–3034, doi: 10.1109/IGARSS39084.2020.9323887.

[23] S. V. Nghiem, R. Kwok, S. H. Yueh, and M. R. Drinkwater, "Polarimetric signatures of sea ice 1. Theoretical model," *J. Geophys. Res.*, vol. 100, no. C7, pp. 13665–13679, 1995, doi: 10.1029/95jc00937.

[24] S. V. Nghiem, R. Kwok, S. H. Yueh, and M. R. Drinkwater, "Polarimetric signatures of sea ice 2. Experimental observations," *J. Geophys. Res.*, vol. 100, no. C7, pp. 13681–13698, 1995, doi: 10.1029/95jc00938.

[25] J. C. Landy, D. Isleifson, A. S. Komarov, and D. G. Barber, "Parameterization of centimeter-scale sea ice surface roughness using terrestrial LiDAR," *IEEE Trans. Geosci. Remote Sens.*, vol. 53, no. 3, pp. 1271–1286, Mar. 2015, doi: 10.1109/TGRS.2014.2336833.

[26] L. Alvarez-Aviles, W. R. Simpson, T. A. Douglas, M. Sturm, D. Perovich, and F. Domine, "Frost flower chemical composition during growth and its implications for aerosol production and bromine activation," *J. Geophys. Res.*, vol. 113, no. D21, pp. 1–10, 2008, doi: 10.1029/2008JD010277.

[27] D. Dickins, "Behavior of oil spills in ice and implications for Arctic spill response," in *Proc. Soc. Petroleum Eng.-Arctic Technol. Conf.*, vol. 2, 2011, pp. 779–793, doi: 10.4043/22126-ms.

[28] NORCOR Engineering and Research Limited, "The interaction of crude oil with Arctic sea ice," NORCOR, Victoria, BC, Canada, Tech. Rep. 27, 1975. [Online]. Available: https://www.restco.ca/BSPTR/BSP_TR27_NORCOR.pdf

[29] S. Martin, "A field study of brine drainage and oil entrainment in first-year sea ice," *J. Glaciol.*, vol. 22, no. 88, pp. 473–502, 1979, doi: 10.3189/s0022143000014477.

[30] M. Oggier, H. Eicken, J. Wilkinson, C. Petrich, and M. ÒSadnick, "Crude oil migration in sea-ice: Laboratory studies of constraints on oil mobilization and seasonal evolution," *Cold Regions Sci. Technol.*, vol. 174, Jun. 2020, Art. no. 102924, doi: 10.1016/j.coldregions.2019.102924.

[31] J. Wilkinson *et al.*, "Oil spill response capabilities and technologies for ice-covered Arctic marine waters: A review of recent developments and established practices," *Ambio*, vol. 46, pp. 423–441, Dec. 2017, doi: 10.1007/s13280-017-0958-y.

[32] D. S. Desmond *et al.*, "Oil behavior in sea ice: Changes in chemical composition and resultant effect on sea ice dielectrics," *Mar. Pollut. Bull.*, vol. 142, pp. 216–233, May 2019, doi: 10.1016/j.marpolbul.2019.03.021.

[33] D. Saltymakova *et al.*, "Effect of dissolution, evaporation, and photooxidation on crude oil chemical composition, dielectric properties and its radar signature in the Arctic environment," *Mar. Pollut. Bull.*, vol. 151, Feb. 2020, Art. no. 110629, doi: 10.1016/j.marpolbul.2019.110629.

[34] D. Isleifson, B. Hwang, D. Barber, R. Scharien, and L. Shafai, "C-band polarimetric backscattering signatures of newly formed sea ice during fall freeze-up," *IEEE Trans. Geosci. Remote Sens.*, vol. 48, no. 8, pp. 3256–3267, Aug. 2010, doi: 10.1109/TGRS.2010.2043954.

[35] A. M. Johansson, C. Brekke, G. Spreen, and J. A. King, "X-, C-, and L-band SAR signatures of newly formed sea ice in Arctic leads during winter and spring," *Remote Sens. Environ.*, vol. 204, pp. 162–180, Jan. 2018, doi: 10.1016/j.rse.2017.10.032.

[36] D. Isleifson, R. Galley, N. Firoozy, J. Landy, and D. Barber, "Investigations into frost flower physical characteristics and the C-band scattering response," *Remote Sens.*, vol. 10, no. 7, p. 991, Jun. 2018, doi: 10.3390/rs10070991.

[37] F. Ulaby and D. Long, *Microwave Radar and Radiometric Remote Sensing*. Ann Arbor, MI, USA: Univ. Michigan Press, 2014.

[38] D. Isleifson, R. J. Galley, D. G. Barber, J. C. Landy, A. S. Komarov, and L. Shafai, "A study on the C-band polarimetric scattering and physical characteristics of frost flowers on experimental sea ice," *IEEE Trans. Geosci. Remote Sens.*, vol. 52, no. 3, pp. 1787–1798, Mar. 2014, doi: 10.1109/TGRS.2013.2255060.

[39] Z. Gao, N.-X. Geilfus, A. Saiz-Lopez, and F. Wang, "Reproducing springtime Arctic tropospheric ozone depletion events in an outdoor mesocosm sea-ice facility," *Atmos. Chem. Phys. Discuss.*, 2021. [Online]. Available: https://acp.copernicus.org/preprints/acp-2021-157/, doi: 10.5194/acp-2021-157.

[40] G. F. N. Cox and W. F. Weeks, "Equations for determining the gas and brine volumes in sea-ice samples," *J. Glaciol.*, vol. 29, no. 102, pp. 306–316, 1983.

[41] M. Leppäranta and T. Manninen, "The brine and gas content of sea ice with attention to low salinities and high temperatures," *Finnish Inst. Mar. Res. Intern. Rep.*, vol. 2, no. 2, pp. 1–14, 1988.

[42] M. Hallikainen and D. P. Winebrenner, "The physical basis for sea ice remote sensing," in *Microwave Remove Sensing of Sea Ice*, F. D. Carsey, Ed. Washington, DC, USA: American Geoph, 1992, pp. 29–46.

[43] D. S. Desmond *et al.*, "Investigation into the geometry and distribution of oil inclusions in sea ice using non-destructive X-ray microtomography and its implications for remote sensing and mitigation potential," *Mar. Pollut. Bull.*, vol. 173, Dec. 2021, Art. no. 112996, doi: 10.1016/j.marpolbul.2021.112996.

[44] (2020). *CloudCompare [GPL Software]*. [Online]. Available: https://cloudcompare.org/

[45] D. Bergström. (2012). *Surface Generation and Analysis—Matlab Code*. MySimLabs. [Online]. Available: http://www.mysimlabs.com/surface_generation.html

[46] E. Asihene *et al.*, "C-band backscatter of oil-polluted new sea ice in a mesocosm," in *Proc. IEEE 19th Int. Symp. Antenna Technol. Appl. Electromagn.*, Aug. 2021, pp. 1–2, doi: 10.1109/ANTEM51107.2021.9518483.

[47] D. G. Barber, "Microwave remote sensing, sea ice and Arctic climate," *Phys. Canada*, vol. 61, pp. 105–111, Sep. 2005. [Online]. Available: https://home.cc.umanitoba.ca/~dbarber/David_Barber/Remote_Sensing_files/Barber_PiC_2005-1.pdf

[48] D. K. Perovich and J. A. Richter-Menge, "Surface characteristics of lead ice," *J. Geophys. Res.*, vol. 99, no. C8, p. 16341, 1994, doi: 10.1029/94jc01194.

[49] R. J. Galley *et al.*, "Micrometeorological and thermal control of frost flower growth and decay on young sea ice," *Arctic*, vol. 68, no. 1, pp. 79–92, 2015, doi: 10.14430/arctic4457.

[50] R. W. Style and M. G. Worster, "Frost flower formation on sea ice and lake ice," *Geophys. Res. Lett.*, vol. 36, no. 11, Jun. 2009, doi: 10.1029/2009GL037304.

[51] M. Shokr and N. Sinha, *Sea Ice: Physics and Remote Sensing*. Hoboken, NJ, USA: Wiley, 2015.

[52] J. Wilkinson *et al.*, "Detection and quantification of oil under sea ice: The view from below," *Cold Regions Sci. Technol.*, vol. 109, pp. 9–17, Jan. 2015, doi: 10.1016/j.coldregions.2014.08.004.

[53] M. Fingas and C. E. Brown, "Detection of oil in, with, and under ice and snow," in *Handbook of Oil Spill Science and Technology*. Hoboken, NJ, USA: Wiley, 2015, pp. 385–394.

Elvis Asihene (Graduate Student Member, IEEE) received the B.Sc. degree in geological engineering from the University of Mines and Technology, Tarkwa, Ghana, in 2011, and the M.Sc. degree in applied geophysics from the University of Ghana, Accra, Ghana, in 2017. He is currently pursuing the Ph.D. degree in geography with the University of Manitoba, Winnipeg, MB, Canada.

His main areas of research are in arctic science, remote sensing, and geographic information system (GIS). He is particularly interested in using microwave remote sensing to detect oil spills in arctic ice-covered waters. His other research interests include electromagnetic modeling and inversion of sea-ice-related parameters, as well as the application of polarimetry and interferometry radar for target characterization and surface subsidence, respectively.

Durell S. Desmond received the B.Sc. degree with a major in physical chemistry and two minors in mathematics, and physics and astronomy and the M.Sc. degree in environment and geography from the University of Manitoba, Winnipeg, MB, Canada, in 2015 and 2018, respectively, where he is currently pursuing the Ph.D. degree in geography.

His research interests lie in remote sensing detection, mitigation, and behavior of oil in sea ice.

Madison L. Harasyn received the B.Sc. degree in physical geography with a certificate in geographic information system (GIS) from Queen's University, Kingston, ON, Canada, in 2017, and the M.Sc. degree in arctic science and remote sensing from the University of Manitoba, Winnipeg, MB, Canada, in 2019.

She is currently a Research Associate with the Centre for Earth Observation Science, University of Manitoba, conducting and assisting with remote sensing and drone-related research throughout the center. Her research interests include the implementation of drones in Arctic-based research, including applying machine learning algorithms to drone imagery and video, and investigating hydrographic phenomena using remote sensing data of various spatial scales.

David Landry received the B.A. degree (Hons.) in archeology from the University of Toronto, Toronto, ON, Canada, in 2010, and the M.A. and Ph.D. degrees in anthropology from the University of Manitoba, Winnipeg, MB, Canada, in 2013 and 2018, respectively.

He is currently a Research Associate with the Centre for Earth Observation Science, University of Manitoba. His research has focused on the use of noninvasive techniques (i.e., remote sensing and geophysics) to investigate archeological sites in the Canadian Arctic.

Cathrin Veenaas received the B.Sc. degree in applied system science and the M.Sc. degree in environmental systems and resource management from Osnabrück University, Osnabrück, Germany, in 2011 and 2013, respectively, and the Ph.D. degree in computational science and engineering with specialization in chemistry from Umeå University, Umeå, Sweden, in 2018.

She is currently a Post-Doctoral Fellow with Örebro University, Örebro, Sweden, and the Centre for Earth Observation Science (CEOS), University of Manitoba, Winnipeg, MB, Canada.

Amirbahador Mansoori (Student Member, IEEE) received the Bachelor of Applied Science degree in electrical engineering with a minor in telecommunications engineering from the Shahid Beheshti University, Tehran, Iran, in 2017, and the Master of Applied Science degree from the Department of Electrical and Computer Engineering, University of Manitoba, Winnipeg, MB, Canada, in 2021.

His research interests are antenna design, applied electromagnetics, and sea ice remote sensing.

Mark Christopher Fuller received the B.Sc. (Hons.), M.Sc., and Ph.D. degrees from the University of Calgary, Calgary, AB, Canada, in 2005, 2008, and 2015, respectively.

He is currently a Research Scientist studying microwave remote sensing of sea ice at the Cryosphere and Climate Research Group, Department of Geography, University of Calgary.

Gary Stern received the Ph.D. degree in chemistry on mass spectrometry from the University of Manitoba, Winnipeg, MB, Canada, in 1991.

He is currently a Professor with the Centre for Earth Observations Sciences, University of Manitoba. He was involved in the study of environmental pathways of contaminants in Arctic marine and freshwater ecosystems. He is involved in the development of oil detection and remediation technologies, impacts, and the fate of oil spills in Arctic marine environments. He is currently the Co-Lead of the GENICE II project that involves genomics research in oil spill preparedness and emergency response in an Arctic marine environment.

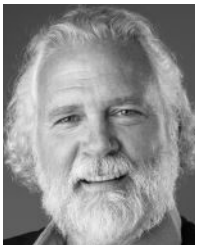

David G. Barber received the Ph.D. degree from the University of Waterloo, Waterloo, ON, Canada, in 1992.

Since 1993, he has been a Professor with the University of Manitoba, Winnipeg, MB, Canada, where he became the Canada Research Chair in Arctic System Science in 2002. He has authored or coauthored over 240 articles and has been a Scientific Leader in large network programs [North Water Polynya (NOW), Canadian Arctic Shelf Exchange Study (CASES), Arctic Network (ArcticNet), Canada Foundation for Innovation (CFL), Bay System (BaySys), and Churchill Marine Observatory (CMO)].

Dr. Barber is also an Invited Member of several national [Natural Sciences and Engineering Research Council Grant Selection Committee (NSERC GSC) 09, NSERC International Polar Year (IPY), and NSERC Northern Supplements) and international [Global Energy and Water Exchanges (GEWEX), International Association of Privacy Professionals (IAPP), Canadian National Committee-Scientific Committee on Oceanic Research (CNC-SCOR), and International Arctic Research Centre (IARC)] committees. He is also a fellow of the Royal Society of Canada (Science Academy), an Officer of the Order of Canada, and a UM Distinguished Professor.

Colin Gilmore (Senior Member, IEEE) is currently the Tier 2 Canada Research Chair in Applied Electromagnetic Inversion and an Assistant Professor of electrical and computer engineering with the University of Manitoba, Winnipeg, MB, Canada. His research interests involve the systems and algorithms of sensing objects with electromagnetic waves, including biomedical imaging for cancer detection and geophysical images to imaging the contents of grain storage bins.

Dustin Isleifson (Senior Member, IEEE) received the B.Sc. degree (Hons.) in electrical engineering and the Ph.D. degree in electrical and computer engineering from the University of Manitoba, Winnipeg, MB, Canada, in 2005, and 2011, respectively.

From 2013 to 2016, he was an Electrical Engineer with the Space Systems Department, Magellan Aerospace, Winnipeg, where he worked on the Radarsat Constellation Mission (RCM). Since 2016, he has been an Assistant Professor with the Department of Electrical and Computer Engineering, in a joint appointment with the Centre for Earth Observation Science (CEOS), University of Manitoba. His research interests include remote sensing, Arctic science, antenna design, and satellite technologies for remote sensing.

Dr. Isleifson was the Conference Co-Chair of IEEE Antenna Technology and Applied Electromagnetics (ANTEM) 2021 and the 19th International Symposium on Antenna Technology and Applied Electromagnetics. He is also the Chapter Chair of the Winnipeg Section of the IEEE Geoscience Remote Sensing/Aerospace and Electronics Systems (GRS/AES).